Aerosol Science and Technology, 39:162–169, 2005

ISSN: 0278-6826 print / 1521-7388 online
DOI: 10.1080/027868290904537

Determination of the Size Distribution of Polydisperse Nanoparticles with Single-Particle Mass Spectrometry: The Role of Ion Kinetic Energy

D. Lee,[1] K. Park,[2] and M. R. Zachariah[2]
[1]*School of Mechanical Engineering, Pusan National University, Geumjeong, Busan, Korea*
[2]*Center for Nanoenergetics Research, Departments of Mechanical Engineering and Chemistry, University of Maryland, College Park, Maryland, USA*

We develop a method to determine size and size distribution (30–150 nm) of polydisperse nanoparticles using a laser ablation/ionization time-of-flight single-particle mass spectrometer that extends the work first described by Reents and Ge. We found a composition independent "power law" dependence between the total peak area and original particle volume that enables one to determine particle volume directly from a particles mass spectrum. This power-law relationship suggests that some ions ablated and ionized from a particle are selectively lost during transport from the laser ablation/ionization region to the detector. A numerical calculation of ion trajectories shows that ion loss is highly dependent on the initial kinetic energy of ions. We show that the size-dependent energetic ions formed by the laser-particle interaction lead to power-law relationship between the cube root of peak area and particle diameter. The results demonstrate that particle size distributions measured with the mass spectrometer are in good agreement with those measured with a scanning mobility particle sizer.

INTRODUCTION

While methods for quantitatively characterizing the size of nanoparticles have advanced considerably in the last decade, the determination of chemical composition is still in relatively infancy, particularly with regard to quantification in a real-time instrument. Ideally one would like to characterize both composition and size simultaneously, and preferably with the same instrument. Such a capability would enable one to conduct a variety of studies on particles in the environment, but it would also open up research opportunities to study gas–particle reactivity (Mahadevan et al. 2002).

Chemical composition of aerosol particles can be determined by traditional off-line methods where particles are collected on a filter or impacted on a substrate for subsequent chemical analysis. However, off-line methods suffer from sampling artifacts such as evaporation of volatile species (negative artifacts) and adsorption/condensation (positive artifacts) that occur when particles are deposited on filter or impactor substrates (Appel 1993). In addition, these techniques are slow and many are generally not appropriate for single-particle analysis.

With this in mind, single-particle mass spectrometry has been a particularly exciting development (Johnston 2000; Mahadevan et al. 2002; McKeown 1991; Salt et al. 1996; Noble and Prather 2000; Reents and Ge 2000). The Prather group (Salt et al. 1996; Noble and Prather 2000) has developed and commercialized a single-particle instrument: aerosol time-of-flight mass spectrometry (ATOFMS) that has a capability of simultaneous measurement of size and composition of a single-particle. However, the lower limit of particle size in the ATOFMS is typically ∼200 nm. Furthermore, this approach does not take advantage of the inherent mass analysis capability of mass spectrometry to determine total particle mass. Instead, the ATOFMS employs a light-scattering/time-of-flight technique to determine particle size, which limits the lower end of the particle sizing range.

Reents and Ge (2000) have studied the potential of using the ion signal from a laser ionization source time-of-flight mass spectrometer to estimate particle mass. In their work they showed that the total peak area in a single-particle mass spectrum can be used to estimate the original particle diameter to within 10%, even though the number of constituent atoms comprising the particle scattered up to ∼34% depending on particle density (refer Table 2 in Reents and Ge 2000). Their size estimation can

Received 25 April 2004; accepted 29 October 2004.
Partial support for this work cam from the DURINT Army Center for NanoEnergetics Research (Dr. D. Mann-program manager). The SPMS was constructed from a National Science Foundation equipment grant (Dr. Mike Roco- program manager). One of the authors, D. Lee was partially supported by Pusan National University Research Resettlement Fund for new faculty member (Project number: 20030278).
Address correspondence to M. R. Zachariah, Departments of Mechanical Engineering and Chemistry, University of Maryland, 2125 Martin Hall, College Park, MD 20742, USA. E-mail: mrz@umd.edu

be justified when two necessary conditions are satisfied. The first is the so called "complete ionization" limit, where all constituent atoms are converted to ions. The second is that the ions should travel from the laser ablation/ionization region to a detector through a time-of-flight (TOF) tube with no losses, and that the detector has no species biases. The first constraint is presumably satisfied with the use of extremely high laser fluences, which are orders of magnitude higher than the theoretical energy necessary to atomize and ionize all the atoms comprising the particle (Reents and Schabel 2001). We have also taken a similar approach. In our previous study, we showed the ability to obtain quantitative elemental analysis for various nanoparticles using a highly focused harmonically doubled, pulsed Nd:YAG laser (Mahadevan et al. 2002). For the ion transport losses, Reents and Ge (2000) reported a linear relationship between the total ion peak area and the monodisperse particle volume. However, they also observed that the size distribution estimated from the total ion peak area was much narrower than the size distribution measured with a scanning mobility particle sizer.

In this work, we also employ a complete fragmentation/ionization technique similar to that of Reents and Ge. We found a composition independent "power law" dependence between the total peak area and original particle volume. We hypothesized that this power-law is related to size-dependent ion loss, which can be attributed to particle size-dependent energetic ion formation during laser ionization. This hypothesis is supported by simulating ion trajectories from the laser focus region to the detector residing at the end of TOF tube, and by estimating the relative ion yields at different initial ion kinetic energies. We show that the deviation from a linear relationship can be interpreted as a particle size-dependent energetic ion formation. Finally, using this relationship we estimate particle size and size distribution of polydisperse NaCl particles from our mass spectrometer, and compare with values measured with a scanning mobility particle sizer (SMPS).

EXPERIMENTAL SECTION

Our single-particle mass spectrometer (SPMS) consists of an aerodynmic inlet region, a source region for particle-to-ions conversion with a free-firing pulsed laser, a TOF region, and a detector, as shown in Figure 1. The aerodynamic lens inlet is employed to separate particles from the carrrier gas and collimate them such that they can be injected with high efficiency through differentially pumped chambers to the ionization region. The pressure in the chamber which houses both the flight tube and the ionization is $\sim 6 \times 10^{-7}$ torr when the aerosol inlet is open.

For ionization we use a frequency-doubled, pulsed Nd:YAG laser operated at 10 Hz in the internal Q-switch mode. A 38 mm focal length lens mounted internal to the vacuum chamber focuses the laser beam that intersects the particle beam. The estimated power density with a laser beam diameter of $\sim$0.3 mm and the laser pulse duration of 5 ns is approximately $\sim 3 \times 10^{10}$ W/cm^2

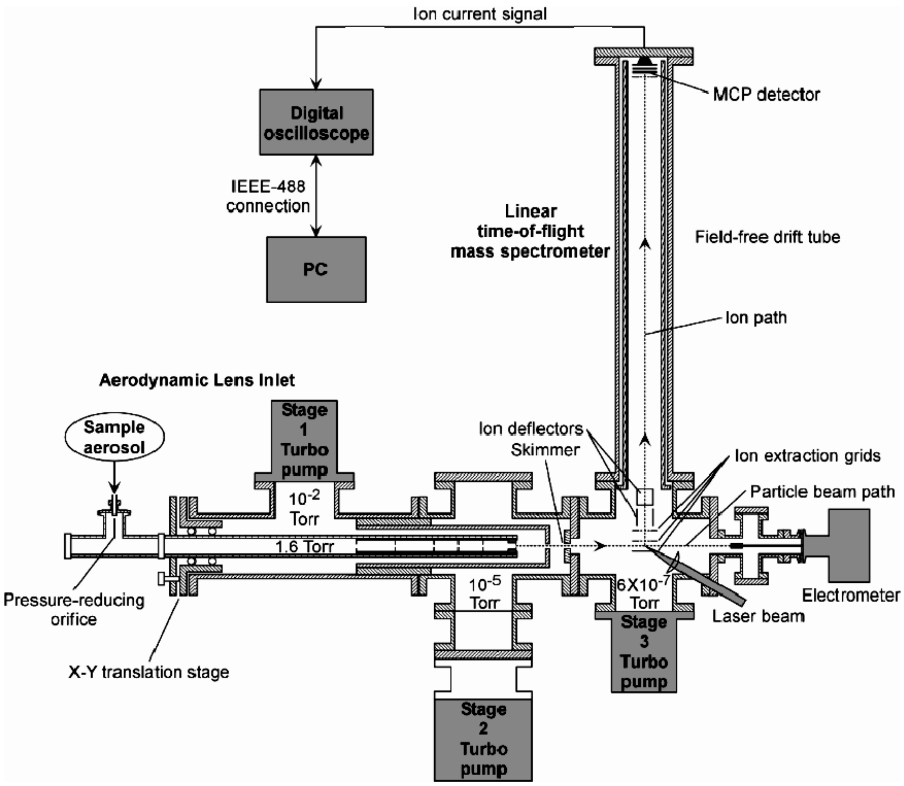

Figure 1. Schematic of SPMS.

at the focal point. The laser energy is maintained above ~100 mJ/pulse to ensure complete fragmentation and ionization of a single particle as determined by threshold ionization (Mahadevan et al. 2002). As configured, positive ions formed by laser ionization are accelerated along ~1 m long linear TOF tube and detected with a microchannel plate (MCP) stack. More complete details of the mass spectrometer are described elsewhere (Mahadevan et al. 2002).

We used sodium chloride nanoparticles as test aerosols. These particles are generated from a 0.2 wt% deionized (DI) water solution using a collison atomizer and were subsequently passed through several diffusion dryers to dry the aerosols. The particle size distribution at the inlet to the aerodynamic lens was measured with a SMPS. The transmission efficiency of the aerodynamic lens was measured using size-selected NaCl particles generated through a differential mobility analyzer (DMA). Size-selected charged particles pass through the aerodynamic lens and the differential pumped chambers, and are collected on an electrode mounted near the point where ionization would take place (Mahadevan et al. 2002). The resulting particle current is measured with an electrometer, and this enables us to estimate the particle size distribution exiting the aerodynamic lens. This corrected particle size distribution exiting the aerodynamic lens is compared with the size distribution inferred from the ion signal intensity.

RESULTS AND DISCUSSION

Mass Spectrometric Determination of Particle Mass

We begin by showing the result that prompts the analysis presented in this article. Figure 2 shows the results for the cube root of the integrated ion current for various particle diameters (50, 70, 120, and 150 nm) selected from the DMA. We are implicitly assuming constant density and a near-spherical particle in order to obtain the correlation between mass and diameter. We present results for three material types, a metal (aluminum), a metal nitrate ($AgNO_3$) and an alkyl halide salt (NaCl). In principle the mass spectrometer's integrated signal is a mass measurement, and Figure 2 should be linear.

In fact, we observe a power law dependence, which interestingly is composition independent, and implies some universally process that is composition invariant. When fitted, one obtains a $d^{0.46}$ dependence instead of unity, $d^{1.0}$.

The remainder of this article seeks to present an explanation of this behavior. Two obvious possibilities exist: (1) we do not completely ionize the larger particles, and (2) there exists some bias such that ions created from larger particles have greater transport losses in the TOF region of the mass spectrometer.

Particle Atomization and Ionization

An example of a typical mass spectrum for a single sodium chloride particle of nominal diameter ~70 nm is shown in Figure 3. With the laser fluencies used we never observe any multiatomic species, while multiply charged atomic ion peaks are commonly observed and are an indicator that ionization efficiency is high. In addition to the signals for Na and Cl we also see H and O, presumably from our inability to completely dry the aerosols. In our prior work we demonstrated that under these conditions relative ion concentration could be determined to within 15% for a variety of different aerosols (Mahadevan et al. 2002). The formation of multiply charged positive ions is not surprising when one considers a simple estimation of the minimum threshold energy required for disintegration/ionization of a NaCl nanoparticle. The minimum energy required to convert

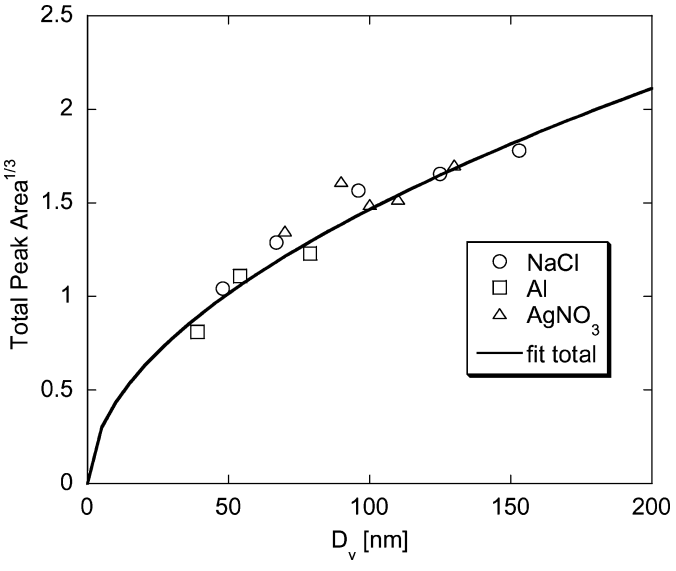

Figure 2. Relationship between the cube root of the integrated signal intensity and particle size for three materials.

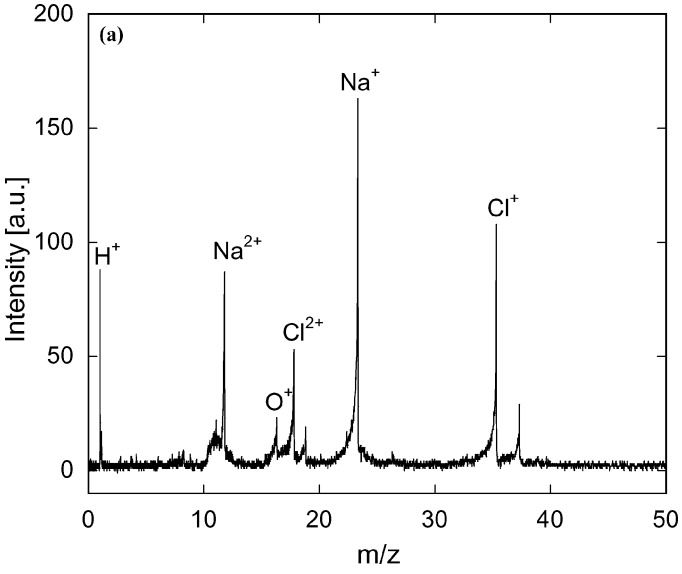

Figure 3. Typical mass spectrum of a NaCl nanoparticle (~70 nm).

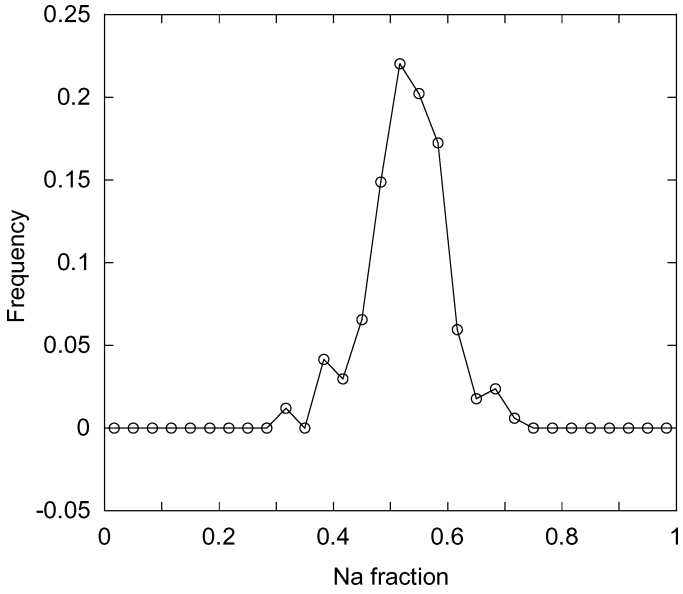

Figure 4. Histogram of Na fraction in polydisperse NaCl nanoparticles.

a 100 nm NaCl particle into Na^+ and Cl^+ is 6×10^{-14} J. For the laser power density disscussed above (100 mJ/pulse) the nominal energy a 100 nm diameter particle is exposed to is 1.1×10^{-8} J (see also Table 3 in Reents and Schabel 2001), or $>5 \times 10^6$ higher than the minimum threshold energy.

Elemental stoichiometric ratios evaluated for 168 sodium chloride particles are indicated in Figure 4. The mode for the atomic sodium fraction (Na/(Na + Cl)) is at 0.516, which is very close to the theoretical value of 0.50. A further indication of the efficient ionization is the invariance in the signal intensity, for 70 nm NaCl particles and 85 nm Al particles (DMA selected) with increasing laser power, as shown in Figure 5.

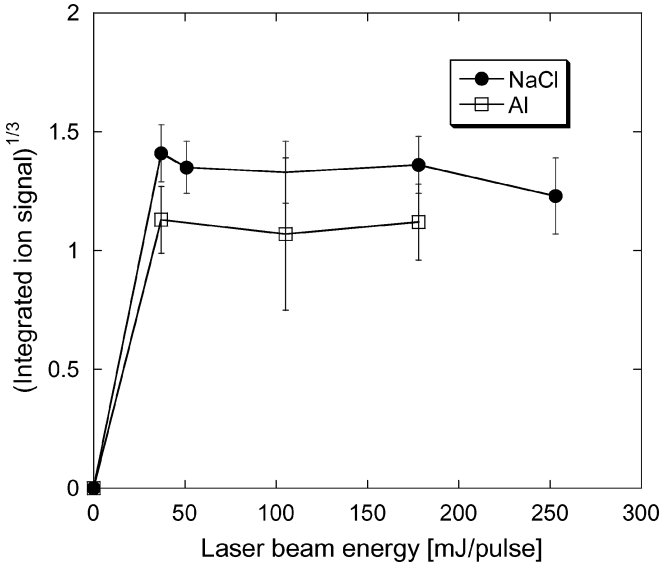

Figure 5. Saturation of ion yield with pulse energy.

Above ~50 mJ/pulse no increase in ion intensity is observed, indicating that the ionization process has been saturated.

The results presented in Figures 3–5 are highly indicative that the ionization process, under the experimental conditions described here, is highly efficient. Transport losses, if they are not ion-specific, would still yield a quantitative stiochiometry determination even if the total mass measurement was in error.

Transport Losses Due to Energetic Ion Formation

Ions were generated from a particle launch toward the detector through three different E-field regions; extraction, acceleration, and the field-free TOF region, as shown in Figure 6a. Following creation some ions will arrive at the detector, while others can be lost at the TOF wall. Here we explore the relative loss of total ions generated as a function of particle size.

The microscopic details of the interaction of an intense laser beam with a particle has been the subject of limited number of experimental and theoretical investigations (Zhigilei et al. 1997; Schoolcraft et al. 2001; Ditmire et al. 1996; Smith et al. 1999; Last and Jortner 2001; Cotter 1994). It is not the purpose of this article to explore the details of that conversion. Rather we assume that the laser–particle interaction leads to a uniformly charged spherical ion cloud of positive ions. The positive ions then undergo expansion due to hydrodynamic and coulomb repulsion (Smith et al. 1999). Ions initially located at the surface will be repelled by all inner charges and internal pressures from the developed plasma, with the outer atoms having the maximum possible kinetic energy (KE) and with the largest population as compared to the inner ions. When particles of different size are converted into their respective ion clouds, under the assumption of a constant cloud density, the cloud size is first-order proportional to original particle size (Smith et al. 1999; Last and Jortner 2001). Based on this, the KE of outer-surface ions dominate the mean KE, and one might assume that they might relate indirectly to the parent particle surface area or at least to some power (α) of the particle size (i.e., KE $\propto d_p^{\alpha}$). In other words, larger particles might generate the more energetic ions. We now turn our attention to how the mean KE affects ion loss. In the following discussion we assume that ion recombination is negligible, which we believe to be a reasonable assumption due to the high extent of ionization observed and the lack of molecular ions.

Figure 6a shows a detailed view of the TOF tube assembly from the laser focus to the MCP detector, while Figure 6b shows the geometric configuration of ions cloud that will be considered in the subsequent calculation. In this model all ions are escaping radially from the cloud, and all voltages, are set for space focusing in the present experimental condition (Cotter 1994). It is reasonable to assume that all forward-ejected ions at zero angle ($\theta = 0^\circ$) (see Figure 6b) will be detected regardless of their initial kinetic energy and have the shortest TOF. On the other hand, backward-ejected ions are decelerated and turn back to the MCP due to the electric field in the extraction region. Thus, backward-ejected ions that are detected have the longest TOF. Furthermore, if we refer to the spectrum in Figure 3,

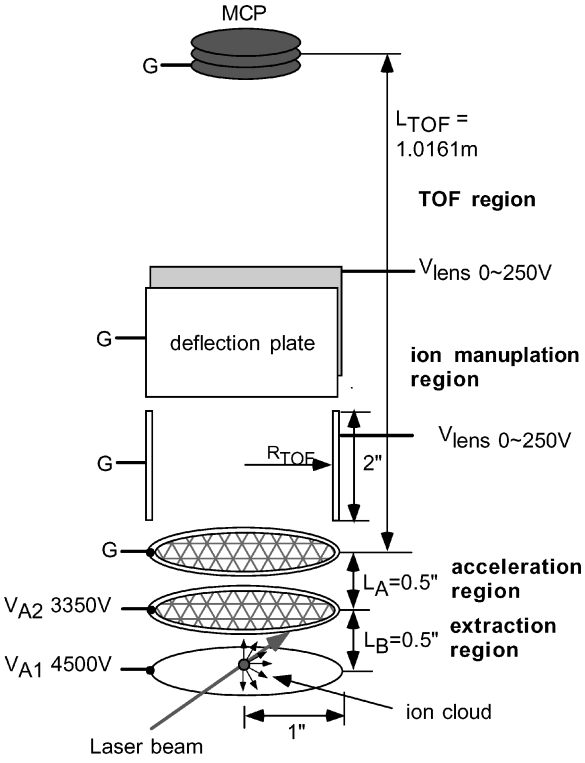

Figure 6. (a) Schematic of TOF tube assembly from ion generation to its detection. (b) Geometrical configuration of ion cloud used in simulation. x denotes the direction toward MCP detector along the centerline of time of flight tube, while y direction is the horizontal direction.

one clearly notices that all peaks are asymmetric with a leading edge that is broad (short TOF) and a trailing edge that is sharp (long TOF). Without resenting all the details this behavior can be simulated and arises from a cloud with a distribution of ion energies. Upward-ejected ions will arrive at times that directly reflect the initial kinetic energy (i.e., higher energy ions will arrive first), and this gives rise to the leading edge distribution. Backward-ejected ions of different kinetic energy, on the other hand, will move away from the detector and will eventually be turned around. Higher energy ions will have a longer flight path because they move away further, but they will also have a longer path to experience the accelerating field once they turn around. As such, backward-ejected ions have the longer TOF but have a flight time that is energy independent, and this is reflected by the very sharp decay in intensity on the trailing edge of a mass peak.

In contrast, horizontally ejected ions at $\theta = 90^\circ$ are most likely to collide with the inner wall of TOF tube and never make it to the detector. Thus, as the ejection angle (θ) increases, ions have are more likely to collide with the wall of TOF. Consequently, a maximum detectable angle $\theta_{\max}$ can be determined by testing if ions ejected at a particular angle with a certain KE arrive at the detector. It is obvious that higher KE might lead to a lower $\theta_{\max}$ and greater ion loss (ion loss $\propto$ KE). By relating this to a power law (KE $\propto d_p^{\alpha}$), we might explain the nonlinear correlation observed in Figure 2. This inference is supported by numerical calculations of ion losses with different initial KEs in the following section.

Modeling Ion Loss from the Laser Focus to Detector

We have constructed a simple model to predict trajectories for ions ejected radially with a mean KE from the laser focus to the MCP. With the axisymmetric nature of ion movements in the linear TOF mass spectrometer (see Figure 6b), the simulation starts with a specified KE [eV], origin ($x = y = 0$), time zero ($t = 0$), and zero angle ($\theta = 0^\circ$). The first step of this simulation is to calculate the external electrostatic forces $\vec{F}$ in the extraction and acceleration regions as shown in Figure 6a. Two components of velocity at time zero (v_{0x} and v_{0y}) are calculated from the KE, θ and ion mass (m): for example, $v_{0x} = \sqrt{2\mathrm{KE}/m}\sin\theta$. The two components of velocity and ion position at the next time step are calculated by simple integration of Newton's equation of motion with time marching:

$$\vec{v}(t+dt) = \vec{v}(t) + \int_t^{t+dt} \vec{F}(t)/m\, dt$$
$$\vec{r}(t+dt) = \vec{r}(t) + \int_t^{t+dt} v(t)dt. \qquad [1]$$

The x component of velocity v_x is invariant in time due to the lack of horizontal force field. We carry out the calculation until the vertical position (y) for an ion reaches the MCP detector. Wall losses of ions are monitored by comparing $|x|$ with the radius of the TOF inner tube (R_{TOF}). When the ions arrived at the detector, the time is recorded as the TOF and comprises the sum of three residence times of ions in the extraction, and acceleration regions, and flight tube (T_B, T_A, and T_{TOF}). For specified electric fields in the three regions (E_B, E_A, and

$E_{\mathrm{TOF}} = 0$), the total TOF of ions ejected at θ with KE is then expressed as follows:

$$\begin{aligned}\mathrm{TOF} = {} & \frac{\sqrt{2m}}{qE_B}\{-\sqrt{\mathrm{KE}}\cos\theta + \sqrt{\mathrm{KE}\cos^2\theta + qE_BL_B/2}\} \\ & + \frac{\sqrt{2m}}{qE_A}\{\sqrt{\mathrm{KE}\cos^2\theta + qE_BL_B/2} \\ & + \sqrt{\mathrm{KE}\cos^2\theta + qE_BL_B/2 + qE_AL_A}\} \\ & + \frac{L_{\mathrm{TOF}}\sqrt{2m}}{2\sqrt{\mathrm{KE}\cos^2\theta + qE_BL_B/2 + qE_AL_A}}, \end{aligned} \quad [2]$$

where q is charge of ion, and subscripts B and A correspond to the regions of extraction and acceleration of ions, respectively.

By increasing the angle to 180°, the model determines whether the ion starting at a certain angle is detectable. This generates a "cone of silence," $\theta_{\mathrm{max},1}$ <90° and $\theta_{\mathrm{max},2}$, >90°, for which between these two angles all ions are lost. Thus, detectable angles are $\theta \le \theta_{\mathrm{max},1}$ and $\theta \ge \theta_{\mathrm{max},2}$. In fact, $180^\circ - \theta_{\mathrm{max},2}$ is close to $\theta_{\mathrm{max},1}$. All ions at the $d\theta$ shell at the surface in Figure 6b should have the same detection efficiency, and their number N_i to that at an angle of zero rapidly increases by a factor of $\sin(\theta_i + d\theta)/\sin(d\theta)$ as the angle θ_i increases (i.e., N_i is directly proportional to the differential area of $d\theta$ shell at the ith angle). Summation of N_i over the effective angle range, and its normalization by the total number of ions, result in the detection efficiency (DE), at a specified value of KE as follows:

$$\mathrm{DE} = \frac{\int_0^{\theta\,\max 1} N_i d\theta + \int_{\theta\,\max 2}^{2\pi} N_i d\theta}{\int_0^{2\pi} N_i d\theta} \quad [3]$$

An outline of the algorithm for the calculation DE is shown in Figure 7. Iteration of the whole procedure with different initial KEs enables us to obtain the DE as a function of the KE as shown in Figure 8. A fit to the result gives a power dependence of the DE on the KE with the exponent of −0.99, implying that that the DE is simply inversely proportional to KE (DE = 16.9 $\mathrm{KE}^{-0.99}$ where the units of DE and KE are percent (%) and eV, respectively). Essentially, the detection efficiency goes as the inverse of the initial kinetic energy, and at the highest ion energies only ions ejected from the polar regions are observed.

One potential method to enhance the transport efficiencies is to employ ion focusing such as with an Einzel lens. Figure 8 also shows an obvious improvement of the detection efficiency for a virtually installed cylindrical Einzel lens as a function of lens voltage. This could be another issue for improvement of ion detectability in the mass spectrometer. Our present configuration does not have provision to install an Einzel system; however, we have been able to apply voltage (V_{lens}) to two sets of deflector plates (see Figure 6a) to search for any evidence for the energetic ion formation. The results presented in Figure 9 show the relative signal intensity as a function of deflector voltage. The increase in

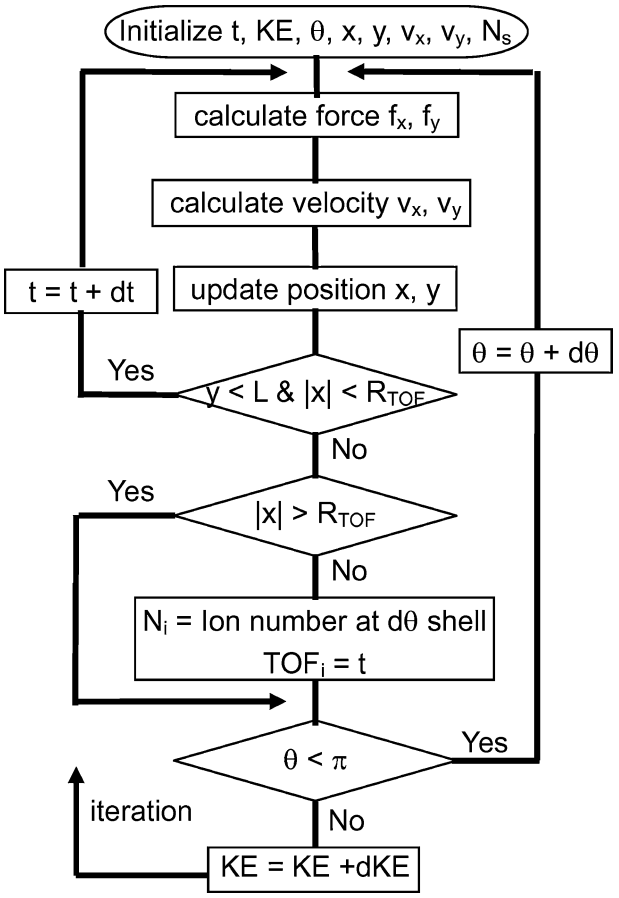

Figure 7. Simulation algorithm for TOF mass spectrum and detection efficiency.

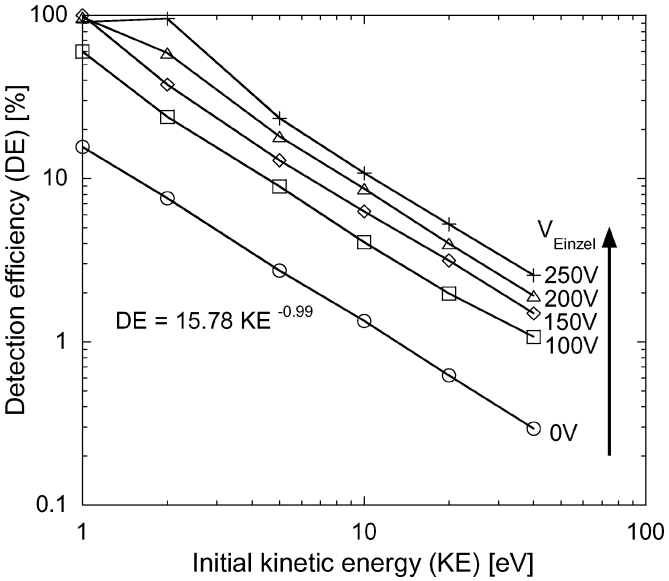

Figure 8. Effect of initial KE on detection efficiency.

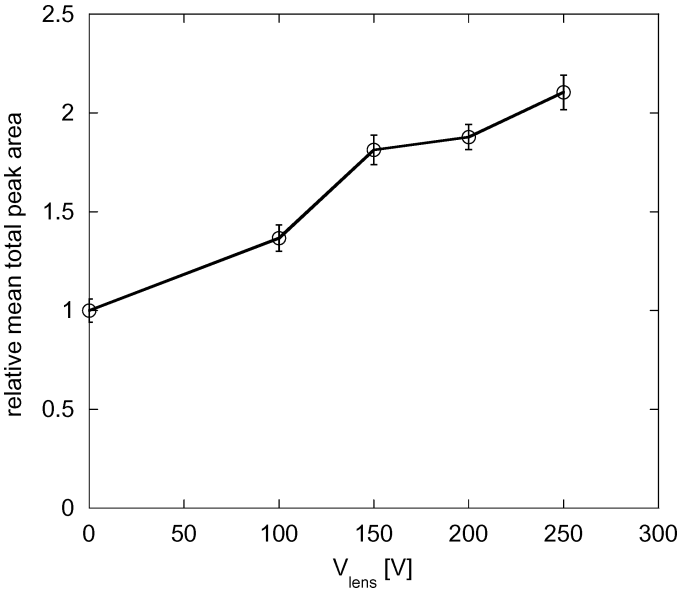

Figure 9. Total ion yield as a function of flight tube steering voltage.

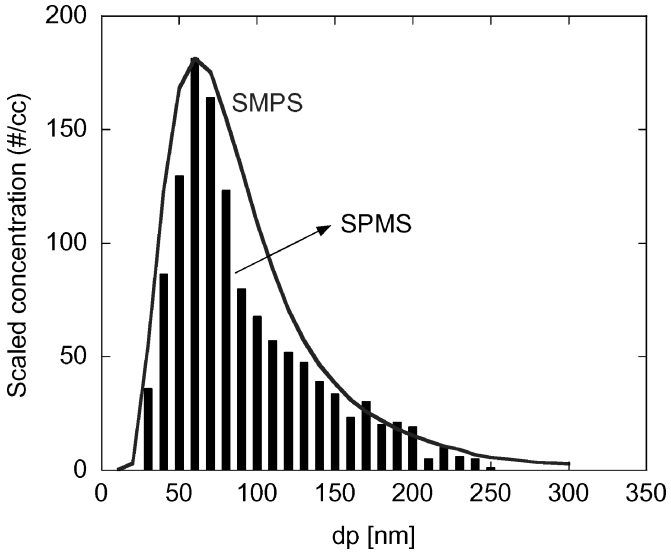

Figure 10. Size distribution as measured by SPMS and comparison with SMPS.

ion intensity is indicative that energetic ions are being lost, and that better extraction and focusing fields—for example, through the use of an Einzel lens—could significantly enhance both the overall sensitivity of the SPMS and perhaps provide a better tool to determine total particle mass.

Size Estimation by Mass Spectrometry

We have obtained two correlations, $\mathrm{KE} \sim d_p^{\alpha}$ and $\mathrm{DE} = 16.9\,\mathrm{KE}^{-0.99}$, yielding $\mathrm{DE} \sim d_p^{-0.99\alpha}$ from the numerical modeling, as described in the previous two sections. The DE in Equation (3) can be also interpreted by the following relation:

$$\mathrm{DE} = \frac{\text{detected ion number}}{\text{total number ofions from a particle}}. \qquad [4]$$

The numerator corresponds to total peak area (TPA) in a mass spectrum, while the denominator at constant density corresponds to the volume of the particle. Thus, the plot of the measured total peak area normalized by the particle volume (d_p^3) against particle size d_p results in the experimental relationship between the DE and d_p. Figure 2 showed that data can be fitted with the equation ($\mathrm{TPA}^{1/3} \sim d_{\mathrm{DMA}}^{0.46}$), leading to $\mathrm{TPA}/d_p^3 \sim d_p^{-1.62} \sim \mathrm{DE}$. Note that mobility size d_{DMA} of NaCl nanocrystals is close to the volume-equivalent size d_p to within 10%. Comparing this with the above relations $\mathrm{DE} \sim d_p^{-0.99\alpha}$ obtained from the numerical modeling, the exponent α is determined to be 1.64. For a surface-sensitive process we would expect a value close to 2, which is reasonably close to our value of 1.64. The absolute differences could be attributed to the assumptions made in the numerical modeling: (1) they initially form a spherical and uniform-charge cloud, and (2) all ions are ejected with a mean KE.

Nevertheless, using the relationship in Figure 2 we obtain a size distribution of polydisperse NaCl particles using the SPMS as shown in Figure 10 and a comparison with particle size distribution obtained with a SMPS. For presentation purposes, the height of the SMPS size distribution is rescaled to match the size distribution obtained from the single-particle mass spectrometer. The figure shows a good agreement between the very different approaches to obtain particle size. The results indicate that one can use the SPMS to obtain quantitative size distribution measurements, and that the total ion current can be correlated to a model that assumes that the KE of the ejected ions is proportional to the particle surface area.

Effects of Ion Mass On Detection Efficiency

Thus far we have addressed the role of ion kinetic energy on ion transmission efficiency and the correlation with particle size. We have yet to deal with a system that contains ions of different masses. Indeed, the ability to measure stoichiometry is critically dependent on this point.

The detection efficiency (DE) is determined by the maximum detectable angle $\theta_{\mathrm{max},1}$. The $\theta_{\mathrm{max},1}$ was defined as the angle at which ions collide with the inner wall of the TOF tube, and can be obtained by the following equation:

$$|x| = v_{0x} * \mathrm{TOF} = \sqrt{2\mathrm{KE}/m}\,\sin\theta_{\mathrm{max},1} * \mathrm{TOF} = R_{\mathrm{TOF}}. \qquad [5]$$

Note that TOF in Equation (2) is proportional to $\mathrm{m}^{1/2}$. Substituting Equation (2) into Equation (5), one can easily show that $\theta_{\mathrm{max},1}$ and the resultant DE are not a function of ion mass m. Therefore, we conclude that for elemental analysis there is no mass bias on transmission efficiency. This is consistent with our experimental observation that we can indeed measure particle stoichiometry with high accuracy (Mahadevan 2002). Recent preliminary

results using a one-dimensional molecular dynamic simulations indicates that the kinetic energy of ions ejected increase with radial position within the ion cloud and is qualitatively consistent with our size-dependent KE assumption. Although the mean KE was only 60% of maximum, the mean in the time evolution of the KE was very close to that of the surface ion KE. Consequently, we conclude that the model assumption employed is reasonable.

CONCLUSION

In this article we report on the use of single-particle mass spectrometry to simultaneously measure both the size and elemental composition of polydisperse nanoparticles. A composition-independent power-law correlation was found between the cube root of the total mass-spectral peak area and particle size. To elucidate the origin of the power law, we used trajectory calculations to determine ion transport losses as a function of initial KE. Combining the nonlinear correlation from experiments with numerical results, we found that the mean KE of ions could be reasoned to be proportional to the surface area of the original nanoparticle.

REFERENCES

Appel, B. R. (1993). Atmospheric Sample Analysis and Sampling Artifacts. In *Aerosol Measurement: Principle, Techniques, and Applications*, edited by K. Willeke and P. A. Baron. Van Nostrand Reinhold, NewYork, pp. 233–259.

Cotter, R. J. (1994). *Time-of-Flight Mass Spectrometry*, ACS Symposium Series 549, American Chemical Society, Washington, DC.

Ditmire, T., Donnelly, T., Rubenchik, A. M., Falcone, R. W., and Perry, M. D. (1996). Interaction of Intense Laser Pulses with Atomic Clusters, *Phys. Rev. A* 53:3379–3402.

Johnston, M. V. (2000). Sampling and Analysis of Individual Particles by Aerosol Mass Spectrometry, *J. Mass Spectrom.* 35:585–595.

Last, I., and Jortner, J. (2001). Nuclear Fusion Induced by Coulomb Explosion of Heteronuclear Clusters, *Phys. Rev. Lett.* 87:033401.

Mahadevan, R., Lee, D., Sakurai, H., and Zachariah, M. R. (2002). Measurement of Condensed-Phase Reaction Kinetics in the Aerosol Phase Using Single Particle Mass Spectrometry, *J. Phys. Chem. A* 106:11083–11092.

McKeown, P. J., Johnston, M. V., and Murphy, D. M. (1991). On-Line Single-Particle Analysis by Laser Desorption Mass Spectrometry, *Analytical Chemistry* 63(18):2069–2073.

Noble, C. A., and Prather, K. A. (2000). Real-Time Single Particle Mass Spectrometry: A Historical Review of a Quarter Century of Chemical Analysis of Aerosols, *Mass Spectrom. Rev.* 19:248–274.

Park, K., Lee, D., Rai, A., Mukherjee, D., and Zachariah, M. R. (2004). Size-Resolved Kinetic Measurements of Aluminum Nanoparticles Oxidation with Single Particle Mass Spectrometry, *J. Phys. Chem. B.* in press.

Reents, W. D., and Ge, Z. (2000). Simultaneous Elemental Composition and Size Distributions of Submicron Particles in Real Time Using Laser Atomization/Ionization Mass Spectrometry, *Aerosol Sci. Tech.* 33:122–134.

Reents, W. D., and Schabel, M. J. (2001). Measurement of Individual Particle Atomic Composition by Aerosol Mass Spectrometry, *Anal. Chem.* 73:5403–5414.

Salt, K., Noble, C. A., and Prather, K. A. (1996). Aerodynamic Particle Sizing Versus Light Scattering Intensity Measurement as Methods for Real-Time Particle Sizing Coupled with Time-of-Flight Mass Spectrometry, *Anal. Chem.* 68:230.

Schoolcraft, T. A., Constable, G. S., Jackson, B., Zhigilei, L. V., and Garrison, B. J. (2001). Molecular Dynamics Simulations of Laser Disintegration of Amorphous Aerosol Particles with Spatially Nonuniform Absorption, *Nucl. Instrum. Meth. B* 180:245–250.

Smith, R. A., Tisch, J. W. G., Ditmire, T., Springate, E., Hay, N., Mason, M. B., Gumbrell, E. T., Comley, A. J., Mountford, L. C., Marangos, J. P., and Hutchinson, M. H. R. (1999). The Generation of High Energy Ions by Photo-Induced Dissociation of Atomic Clusters, *Phys. Scripta* T80:35–39.

Zhigilei, L. V., Kodali, P. B. S., and Garrison, B. J. (1997). Molecular Dynamics Model for Laser Ablation and Desorption of Organic Solids, *J. Phys. Chem. B* 101:2028–2037.